

Confirmation of hot electron preheat with a Cu foam sphere on GEKKO-LFEX laser facility

T. Gong, H. Habara, Y. Uematsu, Y. Hayashi, S. Kawazu, Y. Kubota, T. Matsumoto, S. Nakaguchi, S. Noma, T. Otsuki, A. Tsujii, K. Yahata, Y. Yoshida, Y. Arikawa, S. Fujioka, H. Nagatomo, H. Shiraga, C. McGuffey, C. M. Krauland, M. S. Wei, and K. A. Tanaka

Citation: *Physics of Plasmas* **24**, 112709 (2017);

View online: <https://doi.org/10.1063/1.4999975>

View Table of Contents: <http://aip.scitation.org/toc/php/24/11>

Published by the *American Institute of Physics*

**COMPLETELY
REDESIGNED!**



**PHYSICS
TODAY**

Physics Today Buyer's Guide
Search with a purpose.

Confirmation of hot electron preheat with a Cu foam sphere on GEKKO-LFEX laser facility

T. Gong,¹ H. Habara,^{1,a)} Y. Uematsu,¹ Y. Hayashi,¹ S. Kawazu,¹ Y. Kubota,¹ T. Matsumoto,¹ S. Nakaguchi,¹ S. Noma,¹ T. Otsuki,¹ A. Tsujii,¹ K. Yahata,¹ Y. Yoshida,¹ Y. Arikawa,² S. Fujioka,² H. Nagatomo,² H. Shiraga,² C. McGuffey,³ C. M. Krauland,⁴ M. S. Wei,⁴ and K. A. Tanaka^{1,5,b)}

¹Graduate School of Engineering, Osaka University, 2-1, Yamada-oka, Suita, Osaka 565-0871, Japan

²Institute of Laser Engineering, Osaka University, 2-6 Yamada-oka, Suita, Osaka 565-0871, Japan

³Department of Mechanical and Aerospace Engineering, Center for Energy Research, University of California San Diego, La Jolla, California 92093, USA

⁴General Atomics, San Diego, California 92186-5608, USA

⁵Extreme Light Infrastructure: Nuclear Physics, 30 Reatorului, P.O. Box MG-6, Bucharest, Magurele 077125, Romania

(Received 12 August 2017; accepted 8 November 2017; published online 27 November 2017)

Experiments with a solid Cu foam ($\sim 1.3 \text{ g/cm}^3$) sphere coated by a $20 \mu\text{m}$ CH ablator are performed on the GEKKO-LFEX laser facility to study the effect of hot electron preheat on the implosion performance. When the target is imploded by the GEKKO lasers ($\sim 1.2 \times 10^{15} \text{ W/cm}^2$ in peak intensity), plenty of hot electrons are measured through the induced Cu $K\alpha$ emission, indicating that the target could suffer strong preheat. This suffering of preheat is confirmed by the temporal evolution of the target self-emission, which is well reproduced by a 2D cylindrically symmetric radiative hydrodynamic code (FLASH) when a module handling the hot electron preheat is coupled. The results given by this benchmarked code indicate that, in the typical experiments with a small ($\sim 200 \mu\text{m}$ in diameter) solid sphere target conducted on the GEKKO-LFEX laser facility, the hot electron preheat greatly degrades the implosion performance, reducing the peak areal densities of a Cu foam sphere and a CD sphere by $\sim 20\%$ and $\sim 35\%$, respectively. *Published by AIP Publishing.* <https://doi.org/10.1063/1.4999975>

I. INTRODUCTION

Fast ignition (FI)¹ is a promising approach to realize inertial confinement fusion in laboratory since it relaxes the symmetry requirement of implosion while it has the potential to provide higher energy gains than the conventional central hot-spot scheme.² In this approach, the ignition is triggered by heating the compressed fuel with a “fast” ($\sim \text{MeV}$) electron beam, which is generated by a separate ultra-intense laser (UIL) either in a cone-in-shell concept^{3,4} or in a super-penetration concept.^{5,6} A high-density fuel core plays a key role in this approach, because it determines the number of the fast electrons that can be stopped in the core region and hence the energy of the UIL that can be effectively coupled.

Generally, the high-density fuel core is formed by uniformly irradiating nanosecond pulsed lasers onto a shell target. However, the conventional shell target suffers significant hydrodynamic instability under the current conditions of the GEKKO-XII (GXII) lasers, preventing the creation of a high-density fuel core.^{7,8} Therefore, a mass-equivalent solid deuterated plastic (CD) sphere has been proposed on the GEKKO-LFEX laser facility recently. Although its implosion velocity ($\sim 5 \times 10^6 \text{ cm/s}$) is much smaller than that in the conventional shell target ($\sim 1.2 \times 10^7 \text{ cm/s}$), this solid CD sphere target is more hydrodynamically stable under the converging shock compression; as a result, it becomes increasingly attractive in the experiments where a high-density fuel core is expected.^{7–9}

However, due to the mass-equivalence, the diameter of this solid CD sphere ($\sim 200 \mu\text{m}$) is much smaller than that of the conventional shell target ($\sim 500 \mu\text{m}$). This decrease in the target size will lead to a corresponding decrease in the spot size of drive lasers and hence an increase in the laser intensity if the laser energy and pulse duration are fixed. In typical experiments with this solid CD sphere target, the peak intensity of the drive laser is above 10^{15} W/cm^2 , indicating that a large number of “hot” (suprathermal) electrons could be produced through non-linear laser–plasma interactions (LPIs),¹⁰ such as stimulated Raman scattering (SRS) and two-plasmon decay (TPD). Therefore, hot electron preheat could play an important role in the implosion process.

In this article, we put forward a new type of target, consisting of a solid Cu foam ($\sim 1.3 \text{ g/cm}^3$) sphere coated with a CH layer, to explore the effect of hot electron preheat on the implosion process. Compared with the solid-density Cu sphere used by other researchers,¹¹ this Cu foam sphere has a density much closer to that of the CD sphere ($\sim 1.0 \text{ g/cm}^3$). Therefore, by imploding this Cu foam sphere in the same experimental configuration as that for the CD sphere, similar compression process and hence similar production of hot electrons are expected. When these hot electrons penetrate into the Cu foam, Cu $K\alpha$ line will be stimulated, which provides a direct detection of the hot electrons. With the measured Cu $K\alpha$ intensity, the number of hot electrons can be inferred. Additionally, by conducting the experiment in the super-penetration^{5,6} fast ignition scheme with a separate UIL (the LFEX laser), the implosion degree of the target at

^{a)}Electronic mail: habara@eei.eng.osaka-u.ac.jp

^{b)}Electronic mail: katanaka@eei.eng.osaka-u.ac.jp

different times can be inferred from the additional Cu $K\alpha$ emission induced by fast electrons created with the UIL beam. This implosion degree, together with the measured target self-emission, provides a good detection of the implosion process. All these advantages make the Cu foam target a good platform to study the effect of hot electron preheat on the implosion process.

In our experiments, strong Cu $K\alpha$ emission is measured even without the intense LFEX laser beam, indicating that a large number of hot electrons are produced by the drive lasers and transported into the Cu foam. A rough estimation based on the measured Cu $K\alpha$ intensities shows that more than 27.70 J (0.68% of the drive energy) is transported into the Cu region by the hot electrons, implying that the hot electron preheat could play an important role in the implosion process. The characteristics observed in the temporal evolution of target self-emission are well reproduced by a radiative hydrodynamic code (FLASH¹²) in 2D-cylindrical geometry when a module handling the hot electron preheat is coupled. With the plasma parameters provided by the simulations, the Cu $K\alpha$ emission induced by the fast electron beam is calculated, which agrees well with the experimental data. These results confirm that the hot electron preheat greatly degrades the implosion performance, reducing the peak areal densities of the Cu foam and the CD sphere targets by $\sim 20\%$ and $\sim 35\%$, respectively. Due to its instinctive compression property, this Cu foam target is capable of providing a higher peak areal density than the CD sphere target, making it a good platform to study the energy coupling of a fast electron beam with a high-density core plasma.

The article is arranged as follows: Section II presents the experimental set-up and Sec. III introduces the module developed for handling the hot electron preheat and diagnostics in the simulation. The experimental data and the simulated results are shown and discussed in Sec. IV. Finally, a summary is drawn in Sec. V.

II. EXPERIMENTAL SET-UP

Figure 1 shows the configuration of the experiments performed on the GEKKO-LFEX laser facility. A solid Cu foam sphere [see Fig. 1(b)] with a density of 1.3 g/cm^3 and a diameter of $200 \mu\text{m}$ coated with a $\sim 20 \mu\text{m}$ thick polystyrene (CH) layer is placed at the target chamber center. Twelve GXII laser beams, each operating at a wavelength of 526 nm (2ω) with an energy of $\sim 330 \text{ J}$, are used to uniformly irradiate the target. These lasers are focused with an F/3 lens, resulting in a focal

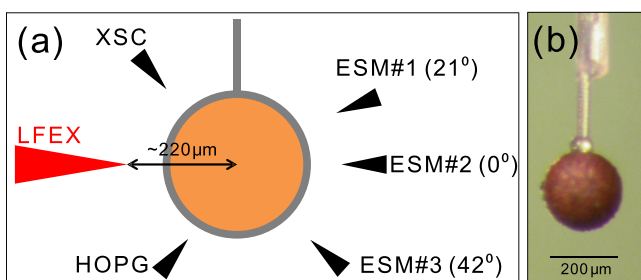


FIG. 1. (a) Experimental set-up and (b) a picture of the Cu foam sphere target.

spot of $\sim 160 \mu\text{m}$ in full width of half maximum (FWHM) at the target surface. The laser pulse shape is Gaussian with an FWHM of 1.3 ns , leading to a peak intensity of $\sim 1.2 \times 10^{15} \text{ W/cm}^2$; consequently, plenty of hot electrons can be produced. Around the time of peak compression, the short pulse (1.5 ps in FWHM) LFEX laser, which operates at a wavelength of 1054 nm (1ω) with an energy of $\sim 1.4 \text{ kJ}$ and a focal spot of $80 \mu\text{m}$, is injected in the equatorial plane. Its focal position is $220 \mu\text{m}$ ahead of the target center [see Fig. 1(a)], which corresponds to the critical density surface at the peak compression as predicted in simulations. With an intensity of $\geq 10^{19} \text{ W/cm}^2$, the LFEX laser is able to generate a forward moving fast electron beam, which provides a novel way to infer the implosion degree through the stimulated Cu $K\alpha$ emission.

Three electron spectrometers (ESMs)¹³ are applied to measure the LFEX generated fast electrons from different directions, 0° (on-axis), 21° and 42° with respect to the LFEX axis. A highly oriented pyrolytic graphite (HOPG) crystal spectrometer serves to measure the Cu $K\alpha$ emission induced by both the GXII produced hot electrons and the LFEX produced fast electrons. Another X-ray streak camera (XSC) functions to monitor the target self-emission, which directly reveals the compression process.

Two types of experiments are performed. In the first type (GXII only shot), the LFEX laser is switched off, so that the measured Cu $K\alpha$ emission provides an estimation of the number of hot electrons penetrating into the Cu foam region. While in the second type (joint shot) where the LFEX laser is injected at different times, the total Cu $K\alpha$ emission is recorded. By subtracting the contribution of the hot electrons from the total emission, the fast electron induced Cu $K\alpha$ emission can be obtained. The measured thickness of the CH layer (τ_{CH}), total energy of the GXII lasers (E_{GXII}), energy of the LFEX laser (E_{LFEX}), delay of the LFEX laser relative to the peak of GXII laser pulse (Δt), and measured Cu $K\alpha$ photons ($I_{\text{K}\alpha}$) for each shot are summarized in Table I. As will be shown later, the variation in the CH thickness leads to a large fluctuation in the hot electron induced Cu $K\alpha$ emission, because the number of the hot electrons penetrating into the Cu foam is found to be well controlled by changing the thickness of the CH layer. The delay of the LFEX laser is obtained by combining the measured and the simulated XSC results, which will be introduced in Sec. IV.

III. PREHEAT MODULE AND DIAGNOSTICS IN THE SIMULATION

Simulations for our experiments are performed with the FLASH code¹² in 2D-cylindrical geometry. The simulation domain is $0 \leq r \leq 500 \mu\text{m}$, $-500 \mu\text{m} \leq z \leq 500 \mu\text{m}$. With the adaptive mesh refinement grid, the minimum spatial resolution is $\sim 1 \mu\text{m}$. The Cu foam placed at ($r=0$, $z=0$) in the simulation is represented by a porous Cu sphere (solid-density granules with many voids) with an average density of 1.3 g/cm^3 . The porous structure has been demonstrated to have little effect on the implosion performance by comparing with the case of a uniformly distributed low-density Cu sphere. The thickness of the CH layer and the energy of the drive laser for each shot are given by the measurements, as shown in Table I.

TABLE I. Thickness of the CH layer (τ_{CH}), energies of GXII (E_{GXII}), and LFEX (E_{LFEX}) lasers, delay (Δt) of the LFEX laser relative to the peak of GXII laser pulse, and measured Cu K α photons ($I_{\text{K}\alpha}$) for each shot.

Shot #	τ_{CH} (μm)	E_{GXII} (J)	E_{LFEX} (J)	Δt (ns)	$I_{\text{K}\alpha}$ (10^{12} ph/sr)
#39863 (GXII only)	18.7 ± 1.0	4160			$6.89 \pm 30\%$
#39865 (GXII only)	20.7 ± 1.0	4044			$4.34 \pm 30\%$
#39866 (joint shot)	20.7 ± 1.0	3800	1372	1.61 ± 0.05	$6.45 \pm 30\%$
#39869 (joint shot)	20.1 ± 1.0	4036	1105	1.68 ± 0.05	$10.33 \pm 30\%$
#39870 (joint shot)	18.7 ± 1.0	3999	1553	2.06 ± 0.05	$12.15 \pm 30\%$
#39871 (joint shot)	18.5 ± 1.0	3730	1384	0.92 ± 0.05	$8.42 \pm 30\%$

Thanks to the 3D-in-2D ray trace algorithm for the laser energy deposition in FLASH, the twelve GXII lasers are set up using the experimental conditions, including the incident direction, F-number, and spot size. A multigroup (6 groups) radiation diffusion model with tabulated opacity is applied for the radiation transport. The tabulated opacity and the tabulated multi-material equation of state in the simulation are given by IONMIX4.¹⁴ The thermal conduction is calculated using a flux-limited model with the Larsen “square-root” flux limiter: $\kappa_{\text{FL}} = [\kappa_{\text{SH}}^{-2} + (fq_{\text{FS}}/|\nabla T_e|)^{-2}]^{-1/2}$. Here, κ_{FL} is the flux-limited conductivity, κ_{SH} is classical Spitzer-Harm conductivity, q_{FS} is the free streaming heat flux, and T_e is the local electron temperature. f is the flux limiter for artificially inhibiting the free streaming heat flux, which is chosen to be 0.06 in our simulations.

To explore the effect of hot electron preheat on the implosion process, a preheat module is developed to couple with the FLASH simulation. Two diagnostics are also developed to synthesize the target self-emission and the fast electron induced Cu K α emission, so that the simulation can be compared with the experiments.

A. Preheat module

Although hot electrons can be produced in many processes, we focus ourselves on the TPD and SRS processes here. These hot electrons are generated at the $n_c/4$ surface ($n_c \approx 4 \times 10^{21} \text{ cm}^{-3}$ for the 2ω GXII lasers) by each of the drive lasers and then propagate inward. Their energy spectrum at time t is described by a Maxwellian distribution function, $f(E, t) \sim 2\sqrt{E/\pi} \times T_{\text{hot}}^{-3/2}(t) \times \exp[E/T_{\text{hot}}(t)]$, where E is the electron energy. The temperature T_{hot} and the energy flux q_{hot} for the TPD and the SRS produced hot electrons are estimated by the following scaling laws:¹⁵

$$T_{\text{hot}}^{\text{TPD}} = 15.5 + 17.7 \xi^{\text{TPD}} \text{ keV}, \quad (1)$$

$$q_{\text{hot}}^{\text{TPD}} = 0.026I \left[1 - \exp\left(-\sqrt{\xi^{\text{TPD}} - 1}\right) \right]; \quad (2)$$

$$T_{\text{hot}}^{\text{SRS}} = m_e v_{\text{ph}}^2 / 2, \quad (3)$$

$$q_{\text{hot}}^{\text{SRS}} = 0.125I \left[1 - \exp\left(1 - \sqrt[3]{\xi^{\text{SRS}}}\right) \right]. \quad (4)$$

Here, $\xi^{\text{TPD}} = I/I_{\text{th}}^{\text{TPD}}$, $\xi^{\text{SRS}} = I/I_{\text{th}}^{\text{SRS}}$, $I_{\text{th}}^{\text{TPD}} = 8.2 T_{\text{keV}} / (L_{\mu\text{m}} \lambda_{\mu\text{m}})$ PW/cm² and $I_{\text{th}}^{\text{SRS}} = 99.5 / (L_{\mu\text{m}}^2 \lambda_{\mu\text{m}}^2)^{2/3}$ PW/cm² are the threshold intensities for TPD and SRS, respectively, in an inhomogeneous plasma. T_{keV} and $L_{\mu\text{m}}$ are the local plasma

temperature in keV and the local density scale length in μm , respectively. $\lambda_{\mu\text{m}}$ is the laser wavelength in μm . m_e is the electron mass and v_{ph} is the phase velocity of the local electron plasma wave. These scaling laws are obtained either from extensive PIC simulations (for TPD) or from experimental estimates (for SRS). Details can be found in Ref. 15 and references therein. The plasma parameters and the laser intensity (I) at the $n_c/4$ surface are used in these scaling laws. Only when the laser intensity exceeds the threshold intensity for TPD or SRS, the hot electrons are present; otherwise, they are absent. The electron energy E starts from a cutoff energy E_c , at which point the energy flux of the hot electrons equals to that of the local thermal electrons.

For simplicity, the transport and deposition of hot electrons are solved in spherically symmetric geometry in our preheat module. At each time step when hot electrons are present, the plasma parameters from the FLASH simulation are poloidally averaged. Then, the energy fluxes of hot electrons produced by the 12 drive lasers are averaged at the $n_c/4$ surface (r_{LPI}), $\bar{q} = (12 \times q_{\text{beam}} A_{\text{beam}}) / (4\pi r_{\text{LPI}}^2)$, where q_{beam} is the energy flux of hot electrons produced by each beam, and A_{beam} is the beam area. With this average energy flux, the initial spectrum of hot electrons $f(E, t)$ is also obtained, which satisfies $\int_{E_c}^{\infty} f(E, t) E dE = \bar{q}$. Here, $f(E, t) \equiv dN/(dt dA dE)$ is defined as the hot electrons produced per unit time per unit area per unit energy, with a unit of $\text{s}^{-1} \text{cm}^{-2} \text{keV}^{-1}$ in our simulations. The hot electrons move radially inward from the $n_c/4$ surface and lose their energy through binary collision as well as exciting plasma waves. The reflective boundary condition is applied at $r=0$ (the target center) to take into account the hot electrons coming from the opposite direction, while the outflow boundary condition is used at the outer boundary, neglecting the refluxing. Since the temperature of hot electrons is just several tens of keV, the electrons surviving at the outer boundary are actually negligible.

The transport of the hot electrons is described by the stopping power

$$\tilde{S}(E, r) \equiv \left| \frac{dE}{dr} \right| = \eta_{\text{SP}} S(E), \quad (5)$$

$$S(E) = -\frac{2\pi r_e^2 m_e c^2 Z n_i}{\beta^2 \langle \cos \theta \rangle} \left\{ \ln \left[\left(\frac{E}{\hbar \omega_p} \right)^2 \frac{\gamma + 1}{2\gamma^2} \right] + 1 + \frac{1}{8} \left(\frac{\gamma - 1}{\gamma} \right)^2 - \left(\frac{2\gamma - 1}{\gamma^2} \right) \ln 2 \right\}. \quad (6)$$

Here, $S(E)$ is the stopping power along the direction of initial electron velocity, as defined by Eq. (22) in Ref. 16. It is derived by taking into account the energy loss through binary collisions and excitation of plasma waves as well as the effect of scattering of energetic electrons. r_e is the classic electron radius, and c is the speed of light in vacuum. Z and n_i are respectively the charge number and density of ions. $\gamma = 1 + E/(m_e c^2)$, $\beta = (1 - \gamma^{-2})^{1/2}$, and $\hbar\omega_p$ is the plasmon energy. $\langle \cos\theta \rangle$ is the angular moments of the hot electron distribution function, which is introduced due to the scattering effect.¹⁶ Generally, the LPI produced hot electrons have a large initial divergence angle,^{11,15,17} which means that they deposit more quickly along the target radius than a well-collimated electron beam does. To take into account this quick energy deposition, we introduce a parameter, $\eta_{SP} (>1)$, in our model. This parameter determines the energy distribution deposited by the hot electrons inside the target. It is the only free parameter in our simulations and will be constrained by the experimental data.

The produced hot electrons are first divided into multiple groups (200 groups in our simulations) with different energies. Then, Eq. (6) is solved for each group from r_{LPI} to $r=0$. The solution gives the final energy $E'(E, r)$ at position r for a group with an initial energy of E . If E' is below the local plasma temperature (T_e), this group is treated as completely stopped. For the surviving groups ($E' > T_e$) at r , they form the local spectrum of hot electrons, $f_-(E', r)$. The subscript $(-)$ represents that these electrons are moving inward. Similarly, solving Eq. (6) from $r=0$ to the outer boundary for the surviving groups, one obtains the spectrum of outward moving $(+)$ hot electrons, $f_+(E', r)$. By summing up the inward and outward moving components, the total spectrum is obtained as follows:

$$f(E', r) = (r_{LPI}^2/r^2) [f_-(E', r) + f_+(E', r)]. \quad (7)$$

Here, a factor r_{LPI}^2/r^2 is introduced to consider the convergence/divergence in the spherical geometry, so that the energy flux is conserved.

Then, the power deposited per unit volume at r can be calculated from the following formula:

$$P_d(r, t) = \int f(E', r) \times \tilde{S}(E', r) dE'. \quad (8)$$

The divergence of P_d at $r=0$ will not affect the simulation, because the deposited energy around the center is finite. Numerically, $P_d(r=0, t)$ is calculated by extrapolation, whose validity has been confirmed by the simulated results. At each simulation step, the deposited energy $P_d \Delta t$ (with Δt being the current time step) is added up to the internal energy of the plasmas.

We note that the energy converted to the hot electrons is not removed from the laser energy in our model. In the simulations discussed here, the peak power and the total energy of the hot electrons are, respectively, $\sim 4.3\%$ and $\sim 2.6\%$ of those of the drive lasers; therefore, this extra energy in the drive lasers affects little on the simulated results. In our model, all the hot electrons are supposed to move inward

from the point of generation. However, in reality, some of the hot electrons could be scattered out of the inner region before arriving at the target center.¹¹ Therefore, the energy deposition in our model might be overestimated. This energy deposition can be improved in the future by measuring the production of hot electrons through the stimulated hard X-ray bremsstrahlung emission. Additionally, the free parameter, η_{SP} , can also be constrained by the 2D Cu K α image in future experiments.

B. Target self-emission

A key observable characterizing the implosion performance in our experiment is the target self-emission measured by the XSC, which records the X-rays from 1 keV to 10 keV. To compare with the experimental XSC data, a diagnostic is developed in the simulation to synthesize the target self-emission. In our simulations, the bulk of the Cu foam is not ablated (as will be shown later in Fig. 5), and the target self-emission is primarily produced by the fully ionized CH plasmas. Therefore, the local thermodynamic equilibrium (LTE) is assumed in the calculation of target self-emission, so that the emission coefficient satisfies $j(\nu) = \rho \kappa_\nu B(\nu, T)$. Here, ν is the photon energy, ρ is the local mass density, κ_ν is the opacity, and $B(\nu, T)$ is the vacuum black body spectral radiance at temperature T . By taking into account the target opacity and 3D geometry, the intensity of the self-emission recorded by the detector at time t is

$$I(x, t) = \int_{y_1}^{y_2} dy \int_{-\infty}^{\infty} dz \int_{\nu_1}^{\nu_2} d\nu \times j(\nu) \exp\left(-\int_z^{\infty} \rho \kappa_\nu dz'\right) \\ \approx \int_{y_1}^{y_2} dy \int_{-\infty}^{\infty} dz \times \rho \kappa_p P_{\nu_1}^{\nu_2}(T) \exp\left(-\int_z^{\infty} \rho \kappa_p dz'\right), \quad (9)$$

where the z axis is along the normal direction of the detecting plane. y_1 and y_2 are determined by the position of the camera slit projected onto the target. ν_1 ($=1$ keV) and ν_2 ($=10$ keV) are the lower and upper limits of the photon energy detectable by the detector, respectively. κ_p is the Planck mean opacity of the plasmas (Cu, or CH, or their mixture) in the energy range from ν_1 to ν_2 , which can be obtained by the TOPS code.¹⁸ $P_{\nu_1}^{\nu_2}(T) \equiv \int_{\nu_1}^{\nu_2} B(\nu, T) d\nu$.

C. Fast electron induced Cu K α emission

Compared to the low-energy (several tens of keV) hot electrons, the fast electrons have much higher energies (\sim MeV); as a result, the assumption of moving in a straight line for the fast electrons would be more reasonable. Besides, their energy spectrum and angular divergence can be inferred from the experimental data measured by ESMs. Therefore, reliable Cu K α emission induced by the fast electrons can be synthesized with the plasma parameters provided by the simulations. In our calculation, the energy spectra of the fast electrons are obtained by fitting the experimental data with exponential functions, while their angular divergence is estimated by comparing the populations in different directions with an assumption of Gaussian distribution. These fast electrons propagate through the target in a

straight line from the point of generation at the critical density surface ($n_{c,1\omega} \approx 10^{21} \text{ cm}^{-3}$ for the 1ω LFEX laser). Their transport is governed by $dE/dx' = S(E) + S^R(E)$, where x' is along the direction of initial electron velocity, and $S(E)$ is the stopping power mentioned above. Another stopping power $S^R(E)$ is introduced to take into account the radiative energy loss for these high-energy ($\sim \text{MeV}$) electrons. It is calculated by linearly interpolating from the National Institute of Standards and Technology (NIST) tables.¹⁹ Solving this transport equation in a similar way as for the hot electrons, one obtains the energy spectra of the fast electrons in the whole space at the time when the LFEX laser is injected, $f^{\text{fast}}(E', \vec{r})$. Then, the Cu K α photons emitted per unit volume per unit solid angle can be derived

$$n_{K\alpha}(\vec{r}) = \frac{1}{4\pi} \int f^{\text{fast}}(E', \vec{r}) \times \mathcal{H}_{K\alpha}(E', \vec{r}) dE', \quad (10)$$

$$\mathcal{H}_{K\alpha}(E, \vec{r}) = \omega_K P_{K\alpha} n_{\text{Cu}}(\vec{r}) \sigma_K(E). \quad (11)$$

Here, $\mathcal{H}_{K\alpha}$ represents the number of Cu K α photons produced by an electron moving per unit length. $\omega_K = 0.44$ is the fluorescence yield, $P_{K\alpha} = 0.88$ is the probability that a K α photon will be produced.^{20,21} n_{Cu} is the number density of the Cu atoms. σ_K is the K-shell ionization cross section.^{22,23} Projecting this emission onto the detecting plane with the consideration of target opacity and 3D geometry, one obtains the detected Cu K α image, $i_{K\alpha}(x, y)$, which can be compared with experimental data from the Cu K α imager in future experiments. By spatially integrating $i_{K\alpha}(x, y)$ in the detecting plane, the total intensity of the Cu K α emission $I_{K\alpha}^{\text{fast}}$ is obtained, which corresponds to the data recorded by the HOPG spectrometer and will be discussed below. Because the ESMSs used in our experiment are not absolutely calibrated, we focus ourselves in this article on the relative Cu K α intensities in different shots.

IV. RESULTS AND ANALYSIS

Figure 2 shows the time-integrated X-ray spectra measured in the experiment, which include the Cu K α emission, the Cu He α emission, as well as the continuum spectrum from the thermal emission. The Cu He α emission is produced because some Cu plasmas have penetrated into the hot coronal region during the implosion due to hydrodynamic instabilities. With a thicker (20.7 μm) CH layer in shot #39865, fewer Cu plasmas are able to penetrate into the coronal region, resulting in weaker Cu He α emission than that in shot #39863. The fewer Cu plasmas in the coronal region in shot #39865 also explain its weaker continuum spectrum.

Since the Cu K α emission can be stimulated not only by the energetic electrons but also by the energetic photons from the radiation in the coronal region, we need to examine the contribution from the later process. This radiation pumped Cu K α emission can be calculated through the integral $I_R = \int i_c(E) \omega_K P_{K\alpha} (E_{K\alpha}/E) dE$, where E is the photon energy, $i_c(E)$ is the continuum spectrum as shown in Fig. 2, and $E_{K\alpha}$ is the Cu K α photon energy.²⁴ The integral extends upwards from the K edge ($\sim 9 \text{ keV}$). By comparing the calculated intensity with the total measured Cu K α intensity (with

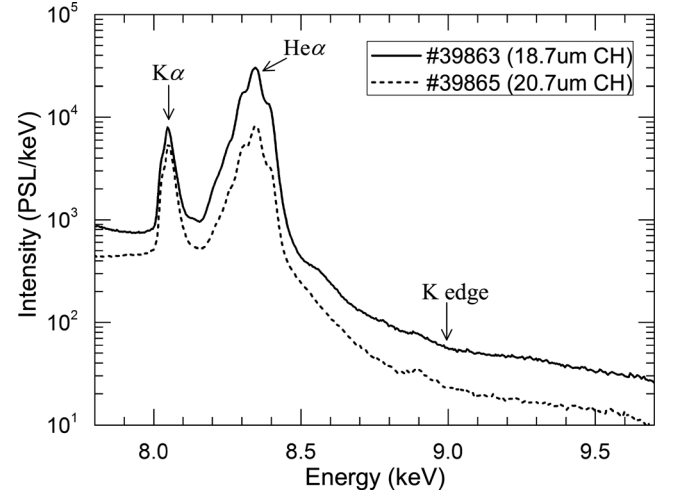


FIG. 2. The X-ray spectra measured by the HOPG spectrometer in the two GXII only shots.

background subtracted), the contribution of the radiation pumped Cu K α emission can be obtained. Relative intensity of the spectrum is enough for this calculation. For the two shots shown in Fig. 2, the calculation indicates that the radiation pumped Cu K α intensities are 1.22% (#39863) and 0.76% (#39865), respectively, of their corresponding total Cu K α intensities. Therefore, the measured Cu K α emission in our experiment is dominated by the contribution from the energetic electrons.

Subtracting the background continuum spectra from the original ones and taking into account the calibration factor $2.01 \times 10^{10} \pm 30\% \text{ ph}/(\text{sr} \cdot \text{PSL})$, one obtains the absolute Cu K α spectra, as shown in Fig. 3. The spectrally integrated intensities are summarized in Table I. As can be seen, the Cu K α intensities in the GXII only shots are comparable within a factor of 2 with those in the joint shots, which indicates that a large number of hot electrons driven by the GXII lasers have penetrated into the Cu foam region during the implosion. To roughly estimate the total energy of hot electrons, we neglect the effect of target opacity and assume that the Cu K α intensity induced by the hot electrons can be approximated by $I_{K\alpha}^{\text{hot}} = (4\pi)^{-1} (\mathcal{E}^{\text{hot}}/\bar{T}^{\text{hot}}) \omega_K P_{K\alpha} \sigma_K(\bar{T}^{\text{hot}}) n_{\text{Cu}} s(\bar{T}^{\text{hot}})$. Here, \mathcal{E}^{hot} and \bar{T}^{hot} are the total energy and average kinetic energy of hot electrons, respectively. $\sigma_K(\bar{T}^{\text{hot}})$ and $s(\bar{T}^{\text{hot}})$ are the K-shell ionization cross section and electron path length at \bar{T}^{hot} , respectively. $\omega_K = 0.44$, $P_{K\alpha} = 0.88$, as defined in Sec. III C. $n_{\text{Cu}} = 1.23 \times 10^{22} \text{ cm}^{-3}$ is the atomic number density of the Cu foam ($1.3 \text{ g}/\text{cm}^3$). For a typical average kinetic energy $\bar{T}^{\text{hot}} = 40 \text{ keV}$, $\sigma_K(\bar{T}^{\text{hot}}) = 4.24 \times 10^{-22} \text{ cm}^2$ according to the cross section given by Hombourger,^{22,23} and $s(\bar{T}^{\text{hot}}) = 6.24 \times 10^{-3} \text{ cm}$ according to the NIST tables.¹⁹ For the Cu K α intensities measured in the two GXII only shots (see Table I), the estimated total energies of hot electrons are 43.98 J (#39863) and 27.70 J (#39865), which correspond to 1.06% and 0.68% of their drive energies, respectively. Note that this estimated total energy is for the hot electrons that have penetrated into the Cu region. In fact, most of the hot electrons are deposited before penetrating through the CH layer. Therefore, their total energy at the point of generation is much larger. This large amount of energy is deposited along

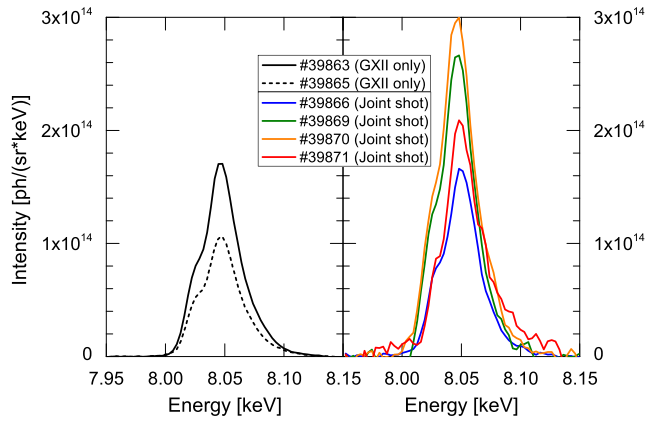


FIG. 3. Cu K α spectra measured by the HOPG spectrometer in (a) GXII only shots and (b) joint shots.

the path of the hot electrons, preheating the target and hence degrading the implosion performance.

Another feature in the Cu K α spectra is the large fluctuation of the intensities between the two GXII only shots (black solid and dashed lines in Fig. 3). Since this Cu K α emission is induced by the hot electrons that have penetrated through the CH layer, the fluctuation could result from the variation in the laser energy (E_{GXII}), which determines the hot electron production, as well as in the CH thickness (τ_{CH}), which determines the decay of hot electron population along the target radius. This sensitive dependence of the penetrated hot electrons on E_{GXII} and τ_{CH} indicates that the hot electron induced Cu K α emission needs to be carefully excluded from the results of joint shots when the fast electron induced Cu K α emission is being calculated. Given this fact, we assume that the total (spectrally integrated) Cu K α intensity induced by the hot electrons satisfies $I_{\text{K}\alpha}^{\text{hot}} = c_1 E_{\text{GXII}} \exp(-c_2 \tau_{\text{CH}})$. The coefficients c_1 and c_2 are derived from the results of the two GXII only shots. Then, the net Cu K α intensity induced by the fast electrons ($I_{\text{K}\alpha}^{\text{fast}}$) is obtained by subtracting this formula from the total intensity in the joint shots. The result for each of the joint shots will be shown later in Fig. 8.

The target preheat implied by the strong Cu K α emission is confirmed by the target self-emission. Figure 4(a) shows a typical result detected by the XSC, in which both the self-

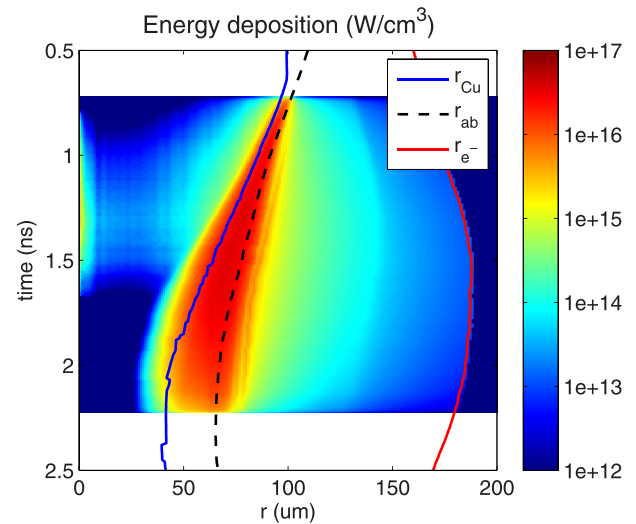


FIG. 5. Temporal and spatial evolution of the power density deposited by hot electrons. The red and blue solid lines represent, respectively, the quarter critical density surface and the interface between Cu foam and the CH layer. The ablation front is also plotted by the black dashed line for reference.

emission and the LFEX induced spike are recorded. As can be seen, the width of the self-emission is almost the same as the initial diameter of the Cu foam ($200 \mu\text{m}$) and does not converge as time proceeds. This “non-converging” feature and the temporal duration ($t_D = 1.07 \text{ ns}$ in FWHM) can be well reproduced by the FLASH simulation ($t_D = 1.10 \text{ ns}$) when the target preheat ($\eta_{\text{SP}} = 6$) is included, as shown in Fig. 4(b). For comparison, the simulated result without the target preheat is presented in Fig. 4(c), in which both a converging behavior and a shorter duration ($t_D = 0.94 \text{ ns}$) can be observed. The weak emission in the central region results from the large opacity of the target.

The effect of hot electron preheat on the implosion process can be found in the power density deposited by the hot electrons (see Fig. 5) and the temporal evolution of plasma parameters (see Fig. 6). The hot electrons are produced from 0.73 ns to 2.22 ns, during which period the drive laser intensity exceeds the thresholds of the LPI processes. With a temperature of $\sim 40 \text{ keV}$, most of the hot electrons are deposited in the CH layer (right side of the blue line in Fig. 5); as a

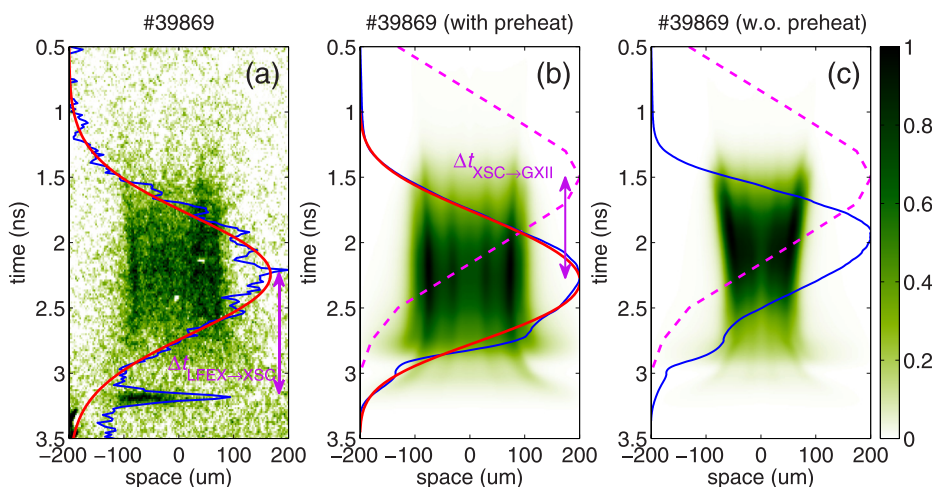


FIG. 4. Target self-emission (a) measured in the experiments and calculated from the simulations (b) with and (c) without hot electron preheat. The power of the self-emission is plotted in blue line and its Gaussian fitting is plotted in red line. The dashed lines in (b) and (c) represent the pulse shapes of GXII lasers in the simulations. A detector resolution of $10 \mu\text{m}$ in FWHM is applied to the calculated results.

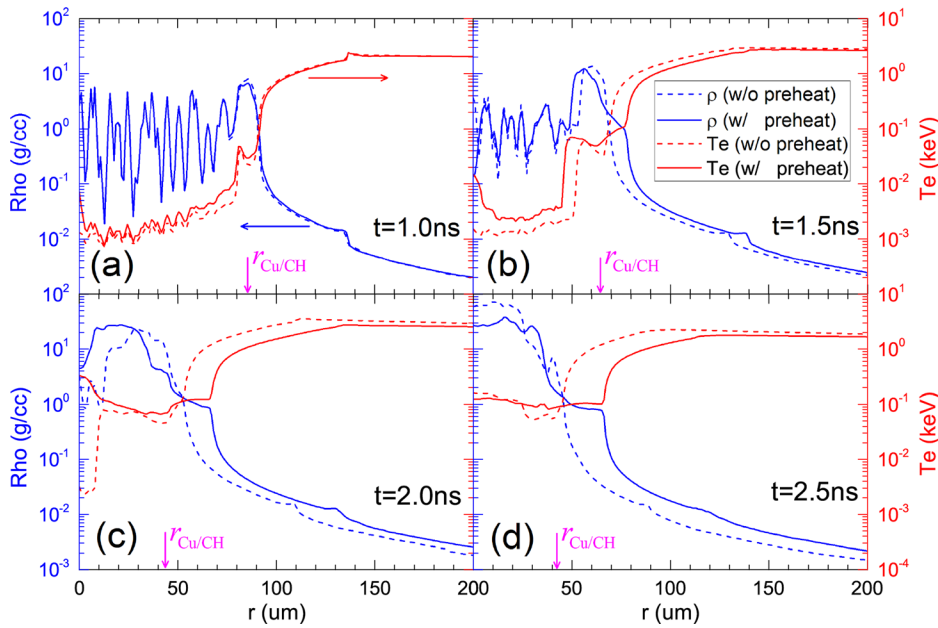


FIG. 6. Spatial distributions of density (blue) and temperature (red) at four different times: (a) 1.0 ns, (b) 1.5 ns, (c) 2.0 ns, and (d) 2.5 ns. Dashed and solid lines represent the results without and with hot electron preheat in the simulations, respectively. The interface between the Cu and CH plasmas in the simulation with hot electron preheat is marked by a magenta arrow.

result, only a few of them (with high energies) are capable of penetrating into the Cu region. This fact could explain the above-mentioned sensitive dependence of hot electron induced Cu K α intensity on the thickness of the CH layer. Figure 5 also shows that the bulk of the Cu foam is not ablated during the implosion, which demonstrates the validity of the LTE assumption in the calculation of target self-emission. The increase in the power density around the center ($r = 0$) results from the spherical convergence. Compared with the case without preheat (dashed blue and dashed red lines in Fig. 6), the hot electron preheat leads to a slight temperature increase (solid red) and a clear density expansion (solid blue) in the shocked region. This density expansion is responsible for the “non-converging” feature observed in the target self-emission [see Fig. 4(b)]. The hot electron preheat also increases the temperature in the inner unshocked region [see red solid lines in Fig. 6(b)]. At almost the same density as that in the case without preheat, this temperature increase results in a larger shock velocity (function of $\sqrt{P/\rho}$, with P being the pressure),¹⁵ as shown by the solid lines in

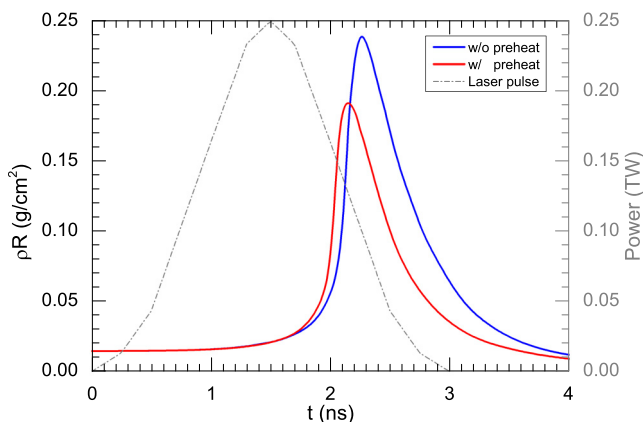


FIG. 7. Temporal evolutions of areal densities for the Cu foam target given by the simulations without (blue) and with (red) hot electron preheat. The power of a single drive laser is plotted in dash dotted for reference.

Fig. 6(b). Although the hot electron preheat could increase the shock pressure, it also decreases the shock strength by raising the local sound velocity,^{15,17} consequently, a smaller peak areal density (0.191 g/cm^2) is achieved compared with that (0.238 g/cm^2) in the case without preheat (see Fig. 7), corresponding to a decrease by 19.8% (or 0.047 g/cm^2). The increase in the shock velocity due to the hot electron preheat is also reflected by the earlier enhancement in the areal density, as shown by the red line in Fig. 7. We note that the oscillation of the density in Fig. 6 originates from the porous structure of the Cu foam target. As the compression proceeds, this oscillation disappears because the voids are occupied by plasmas gradually.

The good agreement of the target self-emission between the simulations (with preheat) and the experiments gives us great confidence to estimate the delay of the LFEX laser relative to the peak of the GXII laser pulse ($\Delta t_{\text{LFEX-GXII}}$). There is no other way to measure this time delay in the

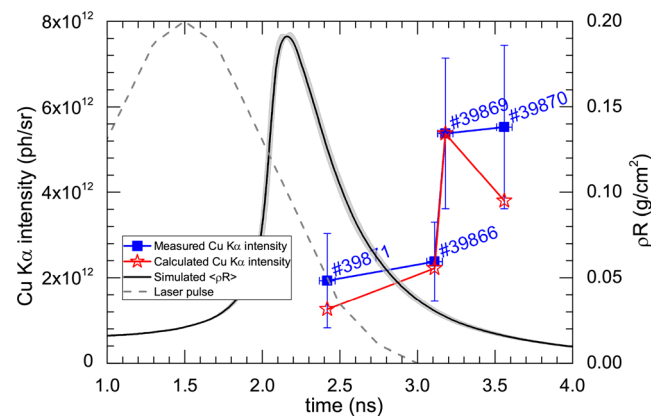


FIG. 8. The fast electron induced Cu K α intensities measured in experiments (blue squares) and calculated from simulations (red stars) as a function of the injection time of the LFEX laser. The calculated results are normalized by the measurement in shot #39869. The areal density (solid black) given by the simulations and the pulse shape of drive lasers (dashed gray) are also plotted for reference. The gray shadow around the areal density represents the fluctuation among the simulated results for the four joint shots.

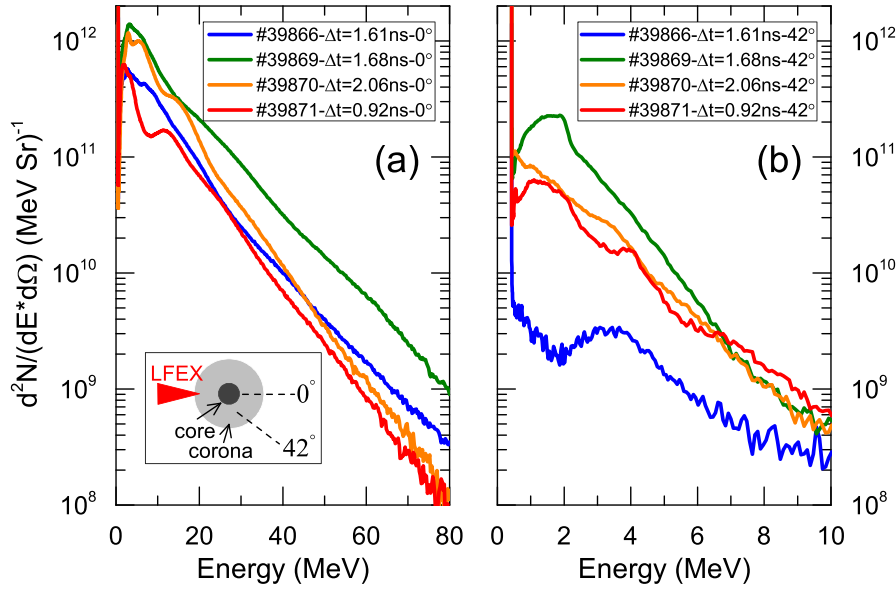


FIG. 9. Energy spectra of fast electrons for each joint shot measured by ESMs at (a) 0° and (b) 42° . The 0° ESM measures the fast electrons passing through the dense core, while the 42° ESM measures the fast electrons passing through the coronal plasmas, as shown in the inset. A clear reduction around 8 MeV at 0° is observed when the LFEX laser is injected around the time of peak compression [#39871, $\Delta t = 0.92$ ns, red line in (a)].

experiment. The estimation is accomplished with the help of the peak self-emission, which is obtained by fitting the self-emission power with a Gaussian function as shown in Figs. 4(a) and 4(b). $\Delta t_{\text{LFEX} \rightarrow \text{GXII}} = \Delta t_{\text{LFEX} \rightarrow \text{XSC}} + \Delta t_{\text{XSC} \rightarrow \text{GXII}}$, where $\Delta t_{\text{LFEX} \rightarrow \text{XSC}}$ and $\Delta t_{\text{XSC} \rightarrow \text{GXII}}$ represent the time differences of the peak self-emission relative to the LFEX laser and to the peak of GXII laser pulse, respectively. The uncertainty of the delay is obtained by varying the best Gaussian fit within the noise of the experimental data.

With the delays of the LFEX laser (see Table I), the fast electron induced Cu K α intensities are obtained as shown by the red stars in Fig. 8, which match the experimental data (blue squares) within the error bars. The experimental data are the net Cu K α intensities induced by the fast electrons, which are derived by the above-mentioned method. The calculated results are normalized by the measurement in shot #39869. The energy spectra and angular divergence of the fast electrons used in the calculation are obtained by fitting the experimental data shown in Fig. 9. By comparing the spectrally integrated intensities at 0° and 42° , the divergence angles (in FWHM) of the fast electrons are estimated, which are 29.9° (#39866), 40.9° (#39869), 34.7° (#39870), and 37.4° (#39871), respectively. Generally, the fast electron induced Cu K α emission is inversely related to the areal

density. This is because the target opacity increases while the emission area decreases with the growth of the areal density. The abnormally high intensity in shot #39869 results from its large production of the fast electrons, as shown by the green lines in Fig. 9. This good agreement of the Cu K α emission between the experimental data and the simulated results again validates the reliability of our simulation. The peak areal density of 0.191 g/cm^2 predicted by the simulation means that a high-density ($\sim 100 \text{ g/cm}^3$) core is achieved by the inward moving shock waves. This high-density core is also supported by the energy deposition of the fast electrons passing through the core. When the LFEX laser is injected around the peak compression (#39871, see Fig. 8), a clear reduction around 8 MeV in the on-axis (0°) energy spectra of fast electrons is observed, as shown by the red line in Fig. 9(a). While in the energy spectra at 42° , which correspond to electrons passing through the coronal plasmas [see the inset in Fig. 9(a)], such reduction is not observed, as shown in Fig. 9(b). Similar results were also reported by Yabuuchi *et al.*²⁵

The benchmarked simulation code is also applied to the CD sphere target. The simulation configurations are the same as those for shot #39869, except that the inner Cu foam sphere is replaced by a uniformly distributed CD sphere with the same average density (1.3 g/cm^3). The simulated results

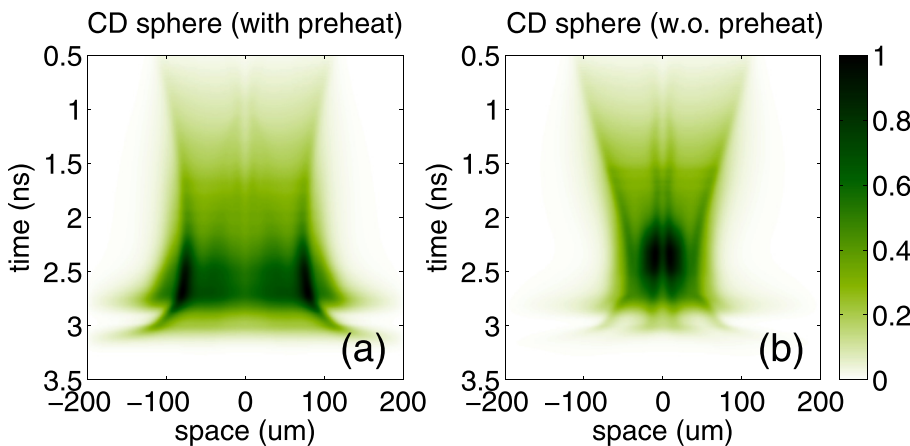


FIG. 10. Target self-emission for the CD sphere target given by the simulations (a) with and (b) without hot electron preheat.

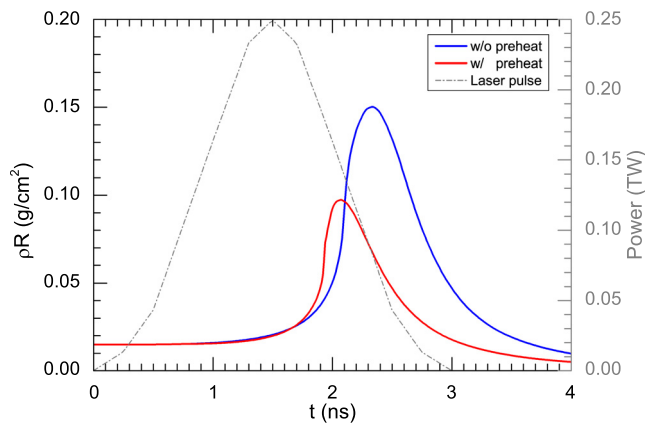


FIG. 11. Same as Fig. 7 but for the CD sphere target.

are shown in Figs. 10 and 11. Similar to what is observed in the Cu foam target, the hot electron preheat in the CD sphere target also leads to a “non-converging” feature in the target self-emission (see Fig. 10), which agrees very well with the data measured by Sawada *et al.*⁹ in an experiment with similar configurations. Because of the hot electron preheat, the peak areal density drops by 35.3% (or 0.053 g/cm^2) from 0.150 g/cm^2 to 0.097 g/cm^2 . The latter is favorably consistent with the result ($\sim 0.07 \text{ g/cm}^2$) reported by Fujioka *et al.*⁸ in their experiments, where a solid CD sphere ($\sim 1.0 \text{ g/cm}^3$, $200 \mu\text{m}$ in diameter, without CH layer) is imploded by only nine GXII laser beams. All these results demonstrate that the hot electron preheat plays an important role in the implosion process, greatly degrading the implosion degree. Therefore, in order to achieve a higher peak areal density, efforts need to be made to suppress the production of hot electrons. Potential methods include decreasing the intensity of drive lasers²⁶ by elongating the pulse duration and raising the thresholds of LPI processes by doping the ablator with high-Z elements.²⁷

The hot electron preheat leads to a greater decrease of peak areal density (35.3% or 0.053 g/cm^2) in the CD sphere target than that (19.8% or 0.047 g/cm^2) in the Cu foam target, because the adiabat increase in the inner region of the former target is larger due to the longer deposition range of hot electrons in this lower-Z material. Whether the hot electron preheat is considered or not, the peak areal density in the Cu foam target is larger than that in the CD sphere target (see Figs. 7 and 11). This is due to their different Hugoniot curves (or equations of state); the material with a higher solid density can be compressed to a higher convergence ratio from a fixed initial density. Therefore, this Cu foam target could be a good platform to study the energy coupling of a fast electron beam with a high-density core plasma. Experiments will be performed in the near future.

This benchmarked simulation code will also be used in the design of our future experiments with a Cu doped CH sphere target. Compared with the Cu foam target, the Cu doped CH sphere target has a smaller opacity for the Cu $K\alpha$ photons; consequently, the transport of fast electrons inside the target could be detected by the Cu $K\alpha$ imager.^{28,29} This transport would benefit the estimation of the energy coupling

efficiency from the short pulse laser to the compressed fuel core.

V. SUMMARY

A novel target, consisting of a Cu foam sphere coated by a CH layer, is applied on the GEKKO-LFEX laser facility to study the effect of hot electron preheat on the implosion performance. Strong Cu $K\alpha$ emission induced by the drive lasers is measured in the experiments, indicating that a large number of hot electrons are produced during the implosion. The measured target self-emission and the fast electron induced Cu $K\alpha$ intensities are well reproduced by the 2D FLASH code when the hot electron preheat is considered, which confirms that the hot electron preheat greatly degrades the implosion performance, reducing the peak areal density in the Cu foam (or CD sphere) target by $\sim 20\%$ (or $\sim 35\%$). Due to its capability of providing a high peak areal density ($\sim 0.2 \text{ g/cm}^2$), the Cu foam target used in this experiment could be a good platform for exploring the energy coupling of a fast electron beam with a high-density core plasma. The benchmarked simulation code will play an important role in the design of our future experiments.

ACKNOWLEDGMENTS

This work was supported by the Grants-in-Aid for Scientific Research (S) from the Japan Society for the Promotion of Science (JSPS) of Japan (Grant No. 15H05751) and the NIFS Collaboration Research Program (Grant Nos. NIFS15KUGK092, NIFS15KNSS060, and NIFS16KUGK103). The software used in this work was in part developed by the DOE NNSA-ASC OASCR Flash Center at the University of Chicago.

¹M. Tabak, J. Hammer, M. E. Glinsky, W. L. Kruer, S. C. Wilks, J. Woodworth, E. M. Campbell, M. D. Perry, and R. J. Mason, *Phys. Plasmas* **1**, 1626 (1994).

²M. Tabak, P. Norreys, V. T. Tikhonchuk, and K. A. Tanaka, *Nucl. Fusion* **54**, 054001 (2014).

³R. Kodama, P. A. Norreys, K. Mima, A. E. Dangor, R. G. Evans, H. Fujita, Y. Kitagawa, K. Krushelnick, T. Miyakoshi, N. Miyanaga, T. Norimatsu, S. J. Rose, T. Shozaki, K. Shigemori, A. Sunahara, M. Tampo, K. A. Tanaka, Y. Toyama, T. Yamanaka, and M. Zepf, *Nature (London)* **412**, 798 (2001).

⁴R. Kodama, H. Shiraga, K. Shigemori, Y. Toyama, S. Fujioka, H. Azechi, H. Fujita, H. Habara, T. Hall, Y. Izawa, T. Jitsuno, Y. Kitagawa, K. M. Krushelnick, K. L. Lancaster, K. Mima, K. Nagai, M. Nakai, H. Nishimura, T. Norimatsu, P. A. Norreys, S. Sakabe, K. A. Tanaka, A. Youssef, M. Zepf, and T. Yamanaka, *Nature (London)* **418**, 933 (2002).

⁵K. Takahashi, R. Kodama, K. A. Tanaka, H. Hashimoto, Y. Kato, K. Mima, F. A. Weber, T. W. Barbee, and L. B. Da Silva, *Phys. Rev. Lett.* **84**, 2405 (2000).

⁶A. L. Lei, A. Pukhov, R. Kodama, T. Yabuuchi, K. Adumi, K. Endo, R. R. Freeman, H. Habara, Y. Kitagawa, K. Kondo, G. R. Kumar, T. Matsuoka, K. Mima, H. Nagatomo, T. Norimatsu, O. Shorokhov, R. Snavely, X. Q. Yang, J. Zheng, and K. A. Tanaka, *Phys. Rev. E* **76**, 066403 (2007).

⁷S. Fujioka, T. Johzaki, Y. Arikawa, Z. Zhang, A. Morace, T. Ikenouchi, T. Ozaki, T. Nagai, Y. Abe, S. Kojima, S. Sakata, H. Inoue, M. Utsugi, S. Hattori, T. Hosoda, S. H. Lee, K. Shigemori, Y. Hironaka, A. Sunahara, H. Sakagami, K. Mima, Y. Fujimoto, K. Yamanoi, T. Norimatsu, S. Tokita, Y. Nakata, J. Kawanaka, T. Jitsuno, N. Miyanaga, M. Nakai, H. Nishimura, H. Shiraga, H. Nagatomo, and H. Azechi, *Phys. Rev. E* **91**, 063102 (2015).

⁸S. Fujioka, Y. Arikawa, S. Kojima, T. Johzaki, H. Nagatomo, H. Sawada, S. H. Lee, T. Shiroto, N. Ohnishi, A. Morace, X. Vaisseau, S. Sakata, Y.

- Abe, K. Matsuo, K. F. Farley Law, S. Tosaki, A. Yogo, K. Shigemori, Y. Hironaka, Z. Zhang, A. Sunahara, T. Ozaki, H. Sakagami, K. Mima, Y. Fujimoto, K. Yamanoi, T. Norimatsu, S. Tokita, Y. Nakata, J. Kawanaka, T. Jitsuno, N. Miyanaga, M. Nakai, H. Nishimura, H. Shiraga, K. Kondo, M. Bailly-Grandvaux, C. Bellei, J. J. Santos, and H. Azechi, *Phys. Plasmas* **23**, 056308 (2016).
- ⁹H. Sawada, S. Lee, T. Shioto, H. Nagatomo, Y. Arikawa, H. Nishimura, T. Ueda, K. Shigemori, A. Sunahara, N. Ohnishi, F. N. Beg, W. Theobald, F. Pérez, P. K. Patel, and S. Fujioka, *Appl. Phys. Lett.* **108**, 254101 (2016).
- ¹⁰W. L. Kruer, *The Physics of Laser Plasma Interactions* (Addison-Wesley, Redwood, 1988).
- ¹¹B. Yaakobi, O. V. Gotchev, R. Betti, and C. Stoeckl, *Phys. Plasmas* **16**, 102703 (2009).
- ¹²B. Fryxell, K. Olson, P. Ricker, F. X. Timmes, M. Zingale, D. Q. Lamb, P. MacNeice, R. Rosner, J. W. Truran, and H. Tufo, *Astrophys. J. Suppl. Ser.* **131**, 273 (2000).
- ¹³K. A. Tanaka, T. Yabuuchi, T. Sato, R. Kodama, Y. Kitagawa, T. Takahashi, T. Ikeda, Y. Honda, and S. Okuda, *Rev. Sci. Instrum.* **76**, 013507 (2005).
- ¹⁴J. J. MacFarlane, *Comput. Phys. Commun.* **56**, 259 (1989).
- ¹⁵A. Colaitis, G. Duchateau, X. Ribeyre, Y. Maheut, G. Boutoux, L. Antonelli, P. Nicolai, D. Batani, and V. Tikhonchuk, *Phys. Rev. E* **92**, 041101 (2015).
- ¹⁶A. A. Solodov and R. Betti, *Phys. Plasmas* **15**, 042707 (2008).
- ¹⁷A. Colaitis, X. Ribeyre, E. Le Bel, G. Duchateau, P. Nicolai, and V. Tikhonchuk, *Phys. Plasmas* **23**, 072703 (2016).
- ¹⁸N. H. Magee, J. Abdallah, R. E. H. Clark, J. S. Cohen, L. A. Collins, G. Csanak, C. J. Fontes, A. Gauger, J. J. Keady, D. P. Kilcrease, and A. L. Merts, "Astrophysical applications of powerful new databases," in *Proceedings of the Astronomical Society of the Pacific Conference Series*, edited by S. J. Adelman and W. L. Wiese (Astronomical Society of the Pacific, San Francisco, 1995), Vol. 78, p. 51.
- ¹⁹See <http://physics.nist.gov/PhysRefData/Star/Text/ESTAR.html> for information about the radiative stopping power.
- ²⁰J. Myatt, W. Theobald, J. A. Delettrez, C. Stoeckl, M. Storm, T. C. Sangster, A. V. Maximov, and R. W. Short, *Phys. Plasmas* **14**, 056301 (2007).
- ²¹W. Bambynek, B. Crasemann, R. W. Fink, H. U. Freund, H. Mark, C. D. Swift, R. E. Price, and P. V. Rao, *Rev. Mod. Phys.* **44**, 716 (1972).
- ²²C. Hombourger, *J. Phys. B* **31**, 3693 (1998).
- ²³J. R. Davies, R. Betti, P. M. Nilson, and A. A. Solodov, *Phys. Plasmas* **20**, 083118 (2013).
- ²⁴B. Yaakobi, A. A. Solodov, J. F. Myatt, J. A. Delettrez, C. Stoeckl, and D. H. Froula, *Phys. Plasmas* **20**, 092706 (2013).
- ²⁵T. Yabuuchi, A. Das, G. R. Kumar, H. Habara, P. K. Kaw, R. Kodama, K. Mima, P. A. Norreys, S. Sengupta, and K. A. Tanaka, *New J. Phys.* **11**, 093031 (2009).
- ²⁶V. A. Smalyuk, D. Shvarts, R. Betti, J. A. Delettrez, D. H. Edgell, V. Y. Glebov, V. N. Goncharov, R. L. McCrory, D. D. Meyerhofer, P. B. Radha, S. P. Regan, T. C. Sangster, W. Seka, S. Skupsky, C. Stoeckl, B. Yaakobi, J. A. Frenje, C. K. Li, R. D. Petrasso, and F. H. Séguin, *Phys. Rev. Lett.* **100**, 185005 (2008).
- ²⁷V. N. Goncharov, T. C. Sangster, P. B. Radha, R. Betti, T. R. Boehly, T. J. B. Collins, R. S. Craxton, J. A. Delettrez, R. Epstein, V. Y. Glebov, S. X. Hu, I. V. Igumenshchev, J. P. Knauer, S. J. Loucks, J. A. Marozas, F. J. Marshall, R. L. McCrory, P. W. McKenty, D. D. Meyerhofer, S. P. Regan, W. Seka, S. Skupsky, V. A. Smalyuk, J. M. Soures, C. Stoeckl, D. Shvarts, J. A. Frenje, R. D. Petrasso, C. K. Li, F. Seguin, W. Manheimer, and D. G. Colombant, *Phys. Plasmas* **15**, 056310 (2008).
- ²⁸M. H. Key, J. C. Adam, K. U. Akli, M. Borghesi, M. H. Chen, R. G. Evans, R. R. Freeman, H. Habara, S. P. Hatchett, J. M. Hill, A. Heron, J. A. King, R. Kodama, K. L. Lancaster, A. J. MacKinnon, P. Patel, T. Phillips, L. Romagnani, R. A. Snavely, R. Stephens, C. Stoeckl, R. Town, Y. Toyama, B. Zhang, M. Zepf, and P. A. Norreys, *Phys. Plasmas* **15**, 022701 (2008).
- ²⁹L. C. Jarrott, M. S. Wei, C. McGuffey, A. A. Solodov, W. Theobald, B. Qiao, C. Stoeckl, R. Betti, H. Chen, J. Delettrez, T. Döppner, E. M. Giraldez, V. Y. Glebov, H. Habara, T. Iwawaki, M. H. Key, R. W. Luo, F. J. Marshall, H. S. McLean, C. Mileham, P. K. Patel, J. J. Santos, H. Sawada, R. B. Stephens, T. Yabuuchi, and F. N. Beg, *Nat. Phys.* **12**, 499 (2016).